




Non-Hermiticity induced exceptional points and skin effect in the Haldane model on a dice latticeRonika Sarkar ¹, Arka Bandyopadhyay ², and Awadhesh Narayan ^{2,*}¹*Department of Physics, Indian Institute of Science, Bangalore 560012, India*²*Solid State and Structural Chemistry Unit, Indian Institute of Science, Bangalore 560012, India*

(Received 10 August 2022; accepted 19 December 2022; published 9 January 2023)

The interplay of topology and non-Hermiticity has led to diverse, exciting manifestations in a plethora of systems. In this work, we systematically investigate the role of non-Hermiticity in the Chern insulating Haldane model on a dice lattice. Due to the presence of a nondispersive flat band, the dice-Haldane model hosts a topologically rich phase diagram with the nontrivial phases accommodating Chern numbers ± 2 . We introduce non-Hermiticity into this model in two ways—through balanced non-Hermitian gain and loss, and by nonreciprocal hopping in one direction. Both these types of non-Hermiticity induce higher-order exceptional points of order three. Remarkably, the exceptional points at high-symmetry points occur at odd integer values of the non-Hermiticity strength in the case of balanced gain and loss, and at odd integer multiples of $1/\sqrt{2}$ for nonreciprocal hopping. We substantiate the presence and the order of these higher-order exceptional points using the phase rigidity and its scaling. Furthermore, we construct a phase diagram to identify and locate the occurrence of these exceptional points in the parameter space. Non-Hermiticity has yet more interesting consequences on a finite-sized lattice. Unlike for balanced gain and loss, in the case of nonreciprocal hopping, the nearest-neighbor lattice system under periodic boundary conditions accommodates a finite, nonzero spectral area in the complex plane. This manifests as the non-Hermitian skin effect when open boundary conditions are invoked. In the more general case of the dice-Haldane lattice model, the non-Hermitian skin effect can be caused by both gain and loss or nonreciprocity. Fascinatingly, the direction of localization of the eigenstates depends on the nature and strength of the non-Hermiticity. We establish the occurrence of the skin effect using the local density of states, inverse participation ratio, and the edge probability and demonstrate its robustness to disorder. Our results place the dice-Haldane model as an exciting platform to explore non-Hermitian physics.

DOI: [10.1103/PhysRevB.107.035403](https://doi.org/10.1103/PhysRevB.107.035403)**I. INTRODUCTION**

In condensed-matter physics, most of the intricate phases of matter, including magnetic and superconducting states, can be understood in the framework of the celebrated Landau theory [1]. However, the two-dimensional electron gas at very low temperatures and under a strong transverse magnetic field exhibits a quantized Hall conductance [2]—such a quantization is not subject to any spontaneous symmetry breaking. Consequently, new concepts have been developed based on single-particle dynamics in topological band theory to unravel the advent of the integer quantum Hall effect. Haldane, in his seminal work, demonstrated that Dirac points in honeycomb lattices such as graphene are protected by both inversion and time-reversal symmetry [3–8]. The absence of any of these symmetries essentially leads to gapped spectra with distinct topological nature. In particular, Semenoff mass assigns an energy offset between the two sublattices of graphene and breaks the inversion symmetry [9]. These inversion symmetry broken systems give rise to the normal or trivial insulators at half filling. In contrast, a staggered magnetic field that turns the second-nearest-neighbor hoppings complex also breaks the time-reversal symmetry of the system without violating

its translational symmetry. These time-reversal symmetry broken Chern insulators are at the heart of realizing quantized transverse Hall conductance in zero external magnetic field condition, namely the quantum anomalous Hall effect. In other words, the Haldane model is an elegant Chern insulator model on a honeycomb lattice that allows tunability between topologically trivial and nontrivial phases by tuning the model parameters. The topological phase diagram of the Haldane model has successfully been realized in experiments using ultracold fermionic atoms in optical lattices [10].

Moreover, unlike graphene, some of the bipartite lattices possess an unequal number of sublattices that offer an intriguing platform to realize perfectly or compact localized states. These compact localized states exhibit nondispersive flat bands, i.e., the energy is independent of momentum in the electronic band structure. The underlying mechanism behind such flat bands can be well explained in terms of destructive interference through various network paths. For example, the bipartite dice lattice [11–20] is one of the first and most prominent examples where such flat-band physics was introduced. In a dice lattice, atoms are not only placed at the vertices of hexagons but also at the centers. Therefore, the number of sites with coordination number three is twice those with coordination number six. In contrast to usual honeycomb lattices, three-component fermions invariably govern the low-energy spectrum of the lattice. The two dispersive bands form Dirac

*awadhesh@iisc.ac.in

cones and touch each other at symmetry points K and K' of the Brillouin zone (BZ), while the remaining one is flat and lies at the Fermi level. The flat bands in the bipartite lattices occur because of the chiral symmetry. In other words, the bipartite model systems (such as dice) with a majority of one kind of sublattice invariably exhibit chiral flat bands [11]. The flat bands have—recently been experimentally realized in photonic crystals employing ultrafast laser technology [21–24]. Motivated by these interesting properties of the dice lattice, the Haldane model has been extended in the form of a three-band model with broken inversion and time-reversal symmetry [25]. As expected, the topological phase diagram of the Haldane dice lattice is richer compared with that of the graphene with more interesting phases both within and outside the topologically nontrivial region [26].

Non-Hermitian physics [27–33], on the other hand, is a topic of growing widespread interest. Non-Hermiticity finds applicability in various fields of photonics, optics, and electronics, among others [34–40]. Since these are open systems, the corresponding non-Hermitian Hamiltonian can accommodate for the gain and loss of particles or energy. Unusual properties, such as complex band spectra and non-orthogonal eigenstates, are the outcomes of such non-Hermitian Hamiltonians [41]. In particular, non-Hermitian systems can show a distinct class of spectral degeneracies known as exceptional points (EPs) [42–53], as well as exceptional contours [54,55]. At an EP the eigenvalues and the eigenvectors simultaneously coalesce making the Hamiltonian defective, i.e., nondiagonalizable. The number of eigenstates undergoing coalescence determines the order of the EP. The study of EPs has gained immense interest in the field of photonic systems [56,57] and microwave cavities [58,59] among others, with interesting applications such as unidirectional sensitivity [60,61], laser mode selectivity [62,63] and optomechanical energy transfer [64]. The non-Hermitian skin effect (NHSE), on the other hand, is a feature unique to non-Hermitian systems where a macroscopic fraction of eigenstates migrate to a boundary of the system as soon as open boundary conditions (OBCs) are imposed [65–74]. This extreme sensitivity of non-Hermitian systems to the boundary conditions leads to an anomalous bulk-boundary correspondence [75–78]. The NHSE has been experimentally observed recently in photonic systems [79], electrical circuits [80,81], and acoustic topological insulators [82,83], among others.

In this paper, we systematically study the interplay between the effect of non-Hermiticity and different kinds of hopping terms in the dice lattice model. Later, we also study the role of disorder [84–93] in the context of the nontrivial effects brought about by non-Hermiticity. We start with only the nearest-neighbor hopping, then subsequently allow complex next-nearest-neighbor hopping terms similar to the Haldane model, and, finally, introduce the inversion-breaking mass terms. For each case, we tune-up a non-Hermitian balanced gain and loss and investigate the changes in the eigenspectra and characterize the EPs which arise. We discover that third-order EPs arise at odd integer values of the non-Hermiticity strength in each case. Their occurrence can be characterized using the phase rigidity which vanishes at the EP. Furthermore, the scaling of phase rigidity with respect to the non-Hermiticity strength helps determine the order of

the EP. When a nonreciprocal hopping is introduced instead of gain and loss, we find that third-order EPs occur at odd integer multiples of $1/\sqrt{2}$. We also elucidate the complete phase diagram to determine the regions where such higher-order EPs can be found in the parameter space. Nonreciprocal hopping has interesting consequences when we consider a finite-sized dice-Haldane nanoribbon. For the dice lattice with only nearest neighbor coupling, under periodic boundary conditions (PBC), the spectrum under nonreciprocal hopping accommodates a finite, nonzero spectral area in the complex plane unlike the gain and loss case where the complex spectrum has an arc-like structure. This finite spectral area results in the occurrence of the NHSE when OBC are imposed on the lattice with nonreciprocal hopping. However, for the dice-Haldane model both gain and loss and nonreciprocal hopping exhibits finite spectral area under PBC and hence displays NHSE under OBC. The direction of the localization can be controlled by the choice of the non-Hermiticity and its strength. We characterize the NHSE using the local density of states, inverse participation ratio (IPR) and the edge probability. This NHSE turns out to be fairly robust to disorder owing to its topological protection. However, at sufficiently large disorder strengths there is a complete destruction of NHSE accompanied by the bulk localization of all the eigenstates.

II. DICE-HALDANE LATTICE MODEL

In this section, we introduce the Haldane model applied to the dice lattice. The system can be viewed as a honeycomb lattice with an additional atom at the center of each hexagonal plaquette, as depicted in Fig. 1(a). Therefore, each unit cell of the lattice possesses three basis atoms denoted by A, B, and C in our work. Among these three lattice sites, A and C are equivalent with coordination number three, while B lattice sites have a coordination number of six. There are two main schemes to obtain dice lattice—using cold atoms confined in optical lattices [14] and growing a trilayer structure of cubic lattices, viz. SrTiO₃-SrIrO₃-SrTiO₃ along the crystallographic (111) direction [15]. Under the tight-binding framework, this model allows the nearest-neighbor (nn) hopping (t) between the sites A-B and B-C. Furthermore, in the spirit of the Haldane model, we consider a complex next-nearest-neighbor (nnn) hopping (t_2) among the A and C lattice sites, such that there is a nonzero flux enclosed by the path formed by the nnn hopping terms. Hence, $t_2 \rightarrow t_2 e^{\pm i\phi}$, where ϕ , $+$, and $-$ indicate staggered flux and the sign of the phase for counterclockwise and clockwise hopping about B lattice sites, respectively. Additionally, a Semenoff mass $+m$ on A and $-m$ on C brings us to the full dice-Haldane lattice model. The complete lattice model and the corresponding BZ are schematically represented in Figs. 1(b) and 1(c), respectively, for convenience (note that for the Hermitian case, $\delta = 0$). The full Hamiltonian of the lattice model can be expressed as follows:

$$H = H_{nn} + H_{nnn} + H_m, \quad (1)$$

where H_{nn} corresponds to the contribution from only nearest-neighbor hopping. In our calculations, we fix $t = 1/\sqrt{2}$, which sets the energy scale of our system. H_{nnn} corresponds to the contribution from next-nearest neighbor hopping

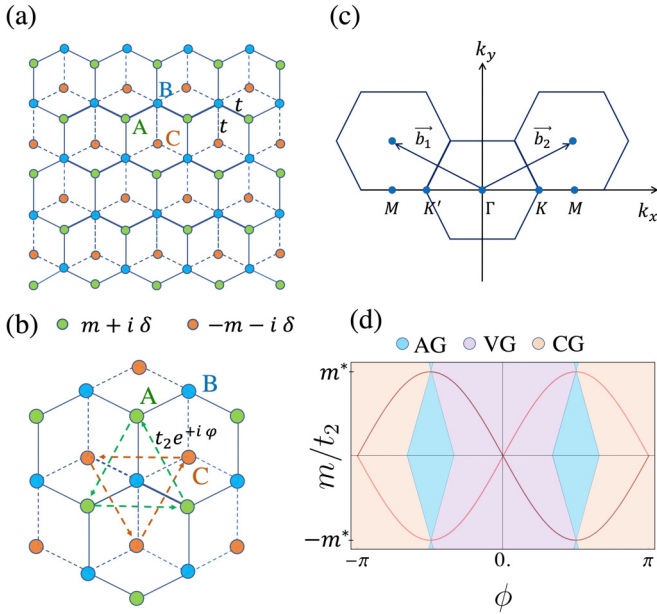


FIG. 1. Illustration of the model, its Brillouin zone, and the Hermitian phase diagram. (a) Schematic of the non-Hermitian dice-Haldane lattice model. A, B, and C are the three sublattice sites. Hopping potential t is the nearest-neighbor hopping between sublattices A-B and B-C. Lattice sites A (shown in green) in general can have a Semenoff mass $+m$ and a non-Hermitian gain $+i\delta$, while lattice sites C (orange) can have a Semenoff mass $-m$ and non-Hermitian loss $-i\delta$. Panel (b) illustrates the next-nearest neighbor Haldane-type hopping with strength t_2 and the flux enclosed by these hopping potentials is ϕ . (c) The BZ of the lattice showing the high-symmetry points M , K' , K , and Γ . (d) The phase diagram of the Hermitian dice-Haldane model where the region enclosed within the curves $\pm m^* \sin \phi$ has a nontrivial Chern number. Outside the curve lies the topologically trivial region. Furthermore, we can find three additional phases—AG: all-gapped (shown in blue), VG: valence-gapped (shown in violet), and CG: conduction-gapped (shown in orange). Here m^* is expressed in units of t_2 .

parameters and H_m to the asymmetric Semenoff mass terms on A and C sites. The expressions for the same are given by

$$\begin{aligned}
 H_{nn} &= t \sum_{\langle i,j \rangle} (c_{A,i}^\dagger c_{B,j} + c_{B,i}^\dagger c_{C,j} + \text{H.c.}), \\
 H_{nnn} &= t_2 e^{\pm i\phi} \sum_{\langle\langle i,j \rangle\rangle} (c_{A,i}^\dagger c_{A,j} + c_{C,i}^\dagger c_{C,j} + \text{H.c.}), \\
 H_m &= m \sum_i (c_{A,i}^\dagger c_{A,i} - c_{C,i}^\dagger c_{C,i}), \quad (2)
 \end{aligned}$$

where c_i^\dagger and c_i represent creation and annihilation operator at the i th lattice site, respectively, and H.c. indicates the Hermitian conjugate partner of the given expression. Moreover, $\langle \cdot \rangle$ and $\langle\langle \cdot \rangle\rangle$ denote nearest neighbors and next-nearest neighbors, respectively. It is needless to mention that H_{nnn} breaks the time-reversal (TR) symmetry in the model without the requirement of a net external magnetic flux, while H_m breaks the inversion symmetry.

The low-energy electronic description of this model can be expressed as a Dirac-Weyl Hamiltonian with pseudospin

equal to one. Both the time-reversal symmetry and inversion-symmetry-broken phases open a gap in the energy spectra. However, these two gapped states are topologically distinct [94,95], classified by different Chern numbers. In other words, the Hermitian dice-Haldane model [26] harbours a richer phase diagram than the conventional Haldane model because the former gives rise to more phases both within and outside the topological region of the usual phase diagram accommodating Chern numbers ± 2 , as shown in Fig. 1(d). Particularly, the topologically nontrivial region is bounded by the relation $m = \pm m^* \sin \phi$ and has a Chern number ± 2 . Due to the bulk-boundary correspondence, two edge modes will appear when open-boundary conditions are invoked. There are additional phases that arise due to the dice lattice structure and its flat band—the all-gapped phase (AG), where all three bands are gapped with no overlap, the valence-gapped phase (VG), where the conduction band and flat band touch each other while the valence band remains gapped, and lastly the conduction-gapped phase (CG) where the conduction band is gapped while the valence and flat bands have some overlap. The electronic band structures of the Hermitian model in the different phases AG, VG, and CG can be found in Appendix A.

III. EFFECT OF NON-HERMITIAN GAIN AND LOSS

Having acquainted ourselves with the Hermitian model, we now systematically invoke non-Hermitian gain and loss and study its interplay with H_{nn} , H_{nnn} , and H_m . Physically, non-Hermitian balanced gain and loss can be thought of as a source attached to one unit-cell atom and an equally strong sink attached to another atom. Here, we allow sublattice A sites to possess a gain $+i\delta$ while sublattice C sites possess a loss $-i\delta$. Hence, the non-Hermiticity added to the Hamiltonian can be described by considering an additional term to Eq. (1), which is of the form

$$H_\delta = i\delta \sum_i (c_{A,i}^\dagger c_{A,i} - c_{C,i}^\dagger c_{C,i}). \quad (3)$$

Here, δ denotes the strength of non-Hermiticity. A point to note is that when we turn off t_2 and m , the Hamiltonian H has parity-time (\mathcal{PT}) symmetry. Any nonzero value of t_2 or m breaks the \mathcal{PT} symmetry.

In this section, we will first consider $H_{nn} + H_{nnn}$ and introduce δ and, thereafter, we study the effect of non-Hermitian gain and loss considering the full Hamiltonian $H = H_{nn} + H_{nnn} + H_m + H_\delta$. For each of these cases, we highlight the exotic physics arising at the high-symmetry points M , K , and Γ , extensively discussing the occurrence of higher-order EPs at integer δ values.

EPs occur when not only two or more eigenvalues become degenerate but also their corresponding eigenvectors [96,97]. This leads to a collapse of the Hilbert space into a lower-dimensional Hilbert space. The collapse of two eigenvectors leads to a second-order EP (EP2). A third-order EP (EP3) occurs upon the collapse of three eigenvectors, and so on. The coalescence of eigenvectors can be characterized by the phase rigidity, which is a measure of the biorthogonality of

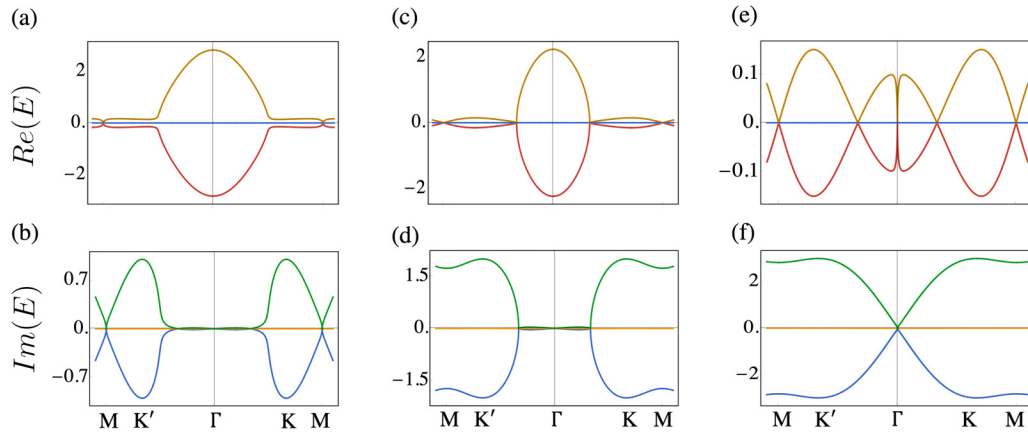


FIG. 2. Spectra with next-nearest-neighbor hopping and non-Hermiticity. The $\text{Re}(E)$ (upper panel) and $\text{Im}(E)$ spectra (lower panel) have been shown for different values of non-Hermiticity strength δ . In panels (a) and (b) $\delta = 1.0$ showing an EP at the M point. In panels (c) and (d) $\delta = 2.0$, this induces an EP at $k_x = 1/3$. In panels (e) and (f) we find an EP at the Γ point for $\delta = 3.0$. For all plots, $t = 1/\sqrt{2}$, $t_2 = 0.06t$, and $\phi = \pi/2$.

the eigenfunctions. It is given by [30,31,53]

$$r_\alpha = \frac{\langle \phi_\alpha | \psi_\alpha \rangle}{\langle \psi_\alpha | \psi_\alpha \rangle}, \quad (4)$$

where ψ_α is the α th right eigenvector of H while ϕ_α is the corresponding left eigenvector of H , i.e., $H|\psi_\alpha\rangle = \lambda_\alpha|\psi_\alpha\rangle$ and $\langle \phi_\alpha|H = \lambda_\alpha\langle \phi_\alpha|$. For a Hermitian system r_α is always equal to unity because the right and left eigenvectors are the same. For non-Hermitian systems, near an EP, $r_\alpha \rightarrow 0$ for the states that coalesce.

Furthermore, to determine the order of the EP, we can perform a scaling analysis of the phase rigidity [98,99]. Here, the Hamiltonian depends on two parameters (k_x , δ). The scaling of phase rigidity follows $|r| \sim |\delta - \delta_{EP}|^\nu$ for an N th order EP, where δ_{EP} is the value of δ for which an EP occurs. It is noteworthy that when an anisotropic EP is approached from two orthogonal directions in parameter space the scaling exponent ν can take values $(N - 1)$ or $(N - 1)/2$ [100,101]. In our case, we fix k_x and investigate the scaling of the phase rigidity with respect to varying non-Hermiticity δ close to the EP. Hence, ν here, is given by $(N - 1)/2$, where N is the order of the EP. In particular, we can plot $\log|r|$ vs $\log|\delta - \delta_{EP}|$ to obtain N from the slope. For example, an EP2 will have a slope of $1/2$, while an EP3 will have a slope of 1 .

In addition to the nearest-neighbor hopping t , first, we include the next-nearest neighbor Haldane type hopping, which breaks time-reversal symmetry of the system. In the presence of a balanced gain and loss term, the Hamiltonian can be written as $H_{nn} + H_{nnn} + H_\delta$. The time-reversal symmetry breaking induces a nontrivial band gap in the Hermitian system (discussed in Appendix A). In other words, the degeneracy at K and K' points is lifted by nonvanishing t_2 (let $\phi = \pi/2$). In the non-Hermitian case, even a small value of δ produces a complex energy spectrum, as expected. Similar to the nearest-neighbor case, finite imaginary parts of the spectra first appear around K and K' points. On the other hand, the conduction and valence bands of the real part of the eigenspectra come closer with increasing δ and finally meet again at M point for $\delta = 1.0$. These observations are illustrated in Figs. 2(a) and 2(b). Furthermore, the degeneracy of $\text{Re}(E)$ at M point is found to

be robust to the values of δ , for $\delta \geq 1$. However, the degeneracy for $\text{Im}(E)$ is lifted beyond $\delta = 1$. With further increase in δ , we have found another set of degeneracies of $\text{Re}(E)$ at the halfway point between $\Gamma \rightarrow K/K'$ for $\delta = 2$. Beyond this value of δ , the degeneracy of $\text{Im}(E)$ at the same ($\pm 1/3, 0$) point is removed [Figs. 2(c) and 2(d)]. It is important to note that the above-mentioned degeneracy of $\text{Re}(E)$ is robust for $\delta \geq 2$, similar to what happens at the M point. Finally, at $\delta \geq 3$, the degeneracy at the Γ point appears and disappears for $\text{Re}(E)$ and $\text{Im}(E)$, respectively, as presented in Figs. 2(e) and 2(f). Similar to the previous cases, the degeneracy of $\text{Re}(E)$ at Γ is robust after this critical point. There occur critical values of δ at which the degeneracy in $\text{Re}(E)$ and $\text{Im}(E)$ exist simultaneously at particular k_x values. Now, we explore the possibility of these points being EPs and their corresponding order at these critical δ values, which are interestingly exact integers. The phase rigidity and its corresponding scaling at M and Γ points are shown in Fig. 3. From the zero value of r_α and the corresponding scaling giving a slope of one, it is clear that all these points are indeed higher-order EPs of order three.

At this point, it is worth exploring the underlying reason behind the emergence of EPs at high-symmetry points due to odd integer values of δ . However, it is possible to get EPs away from high-symmetry points at even values of δ . For this purpose, we have analytically calculated the energy-band dispersion of the nearest-neighbor lattice described by $H_{nn} + H_\delta$. It is evident that the Hamiltonian will give rise to three energy bands including the nondispersive flat band at zero energy. The dispersive bands, on the other hand, have the following expression:

$$E_\pm(k_x, \delta) = \pm\sqrt{3 - \delta^2 + 4\cos(\pi k_x) + 2\cos(2\pi k_x)}. \quad (5)$$

When these bands collapse with the flat band, it gives rise to EPs at specific strengths of non-Hermiticity δ given as below,

$$\delta_{EP} = \pm\sqrt{3 + 4\cos(\pi k_x) + 2\cos(2\pi k_x)}. \quad (6)$$

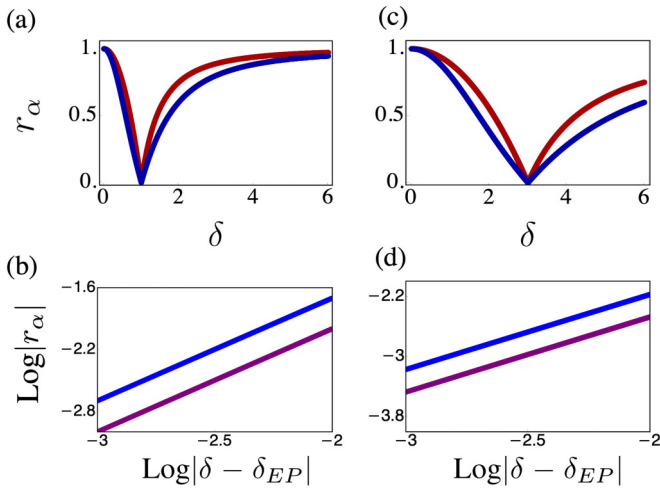


FIG. 3. Phase rigidity for next-nearest-neighbor hopping with non-Hermiticity. The upper panels show the phase rigidity, r_α , as a function of non-Hermiticity, δ , while the lower panels show the scaling of the corresponding r_α . Panels (a) and (b) correspond to the M point, where an EP is induced at $\delta = 1$. Panels (c) and (d) correspond to the Γ point, where another EP is induced at $\delta = 3.0$. The scaling of r_α gives a slope of one in both cases implying the both the EPs are of order three. The different colors in the plots correspond to different eigenstates. The r_α for the two dispersive bands overlap. Here, $t = 1/\sqrt{2}$, $t_2 = 0.06t$, and $\phi = \pi/2$.

Hence, from the solutions of the above equation we see that EP3 arises at $\delta_{EP} = \pm 3$ and $\delta_{EP} = \pm 1$ for the Γ ($k_x = 0$) and M ($k_x = 1$) points, respectively.

Motivated by our above findings, we next add the inversion-breaking Semenoff mass term for setting up the complete dice-Haldane lattice model with the Hamiltonian $H = H_{mn} + H_{nm} + H_m$. We note that the mass term ($+m$ on A lattice sites and $-m$ on C lattice sites) leads to a critical value of m in the units of t_2 ($m = m^* = 0.16$), where a gap-closing occurs at the K point while the K' point remains gapped. Away from this critical m value, the bands become gapped again. In particular, for $m < m^*$, one lies in the nontrivial topological region of the phase diagram whereas, for $m > m^*$ topologically trivial spectra are obtained. The $m = m^* = 0.16$ point corresponds to the semimetallic phase associated with band gap closing only at K but not at K' . Corresponding band diagrams have been detailed in Appendix A.

We next explore the effect of the non-Hermitian gain and loss in both the topologically nontrivial and trivial phases. For this purpose, we first chose a value of m ($m = 0.06$) that satisfies the $m < m^*$ criterion for being topologically nontrivial. Furthermore, we introduce and systematically vary δ to investigate its effect on the complex energy-band structure. We find that the sole variation of non-Hermiticity strength δ can bring about a gap-closed real energy spectrum. This gap closing takes place close to M point for $\delta \approx 1.0$ as presented in Fig. 4(a). Here, the imaginary spectrum is also triply degenerate [Fig. 4(b)], which subsequently gaps out. Hence, we find a third-order EP at $k_x = 1.07$ for $\delta_{EP} = 0.94$. The scaling of the phase rigidity around this EP is shown in Fig. 4(c), confirming its nature. Furthermore, we choose m ($m > m^*$) such that we start from the topologically trivial phase and then invoke non-Hermiticity. In this condition the $\text{Re}(E)$ spectra never undergo band closing, and thus EPs cannot emerge, even for arbitrarily large values of δ . Therefore, we have discovered that inversion symmetry breaking in the dice Haldane model offers an EP near the M point only in the topologically nontrivial case. On the other hand, an EP at Γ point can be obtained primarily in the inversion-symmetric conditions, i.e., $m = 0$. For better understanding, the complete phase diagram for the emergence of EPs at the Γ and M points in the parameter space of the model is presented in Fig. 5(a) and 5(b), respectively. The regions in the parameter space where the phase rigidity approaches zero are the regions where EPs can be found. We observe extended regions with phase rigidity values very close to zero. This indicates that fine tuning of parameters δ and m/t_2 is not required to obtain these exceptional regions expanding the possibilities for reaching low values of phase rigidity [102]. The occurrence of EPs also signify a topological phase transition as these are regions of band-gap closing. It is important to note that these phase transitions are possible only at low values of m ($m < m^*$). This follows from our prior observation that gap closings cannot occur solely due to non-Hermiticity unless we are in the topologically nontrivial region of the Hermitian model. In contrast to the conventional Haldane model, the topological phase transition is now driven by a complex mass term. In particular, the edge states that usually occur in the Hermitian topological phase of Haldane model are also observed in the presence of gain and loss (δ). However, the topological protection of the edge states in the \mathcal{PT} -symmetry-broken phase holds only up to a critical value of δ . This phase transition is associated with passing

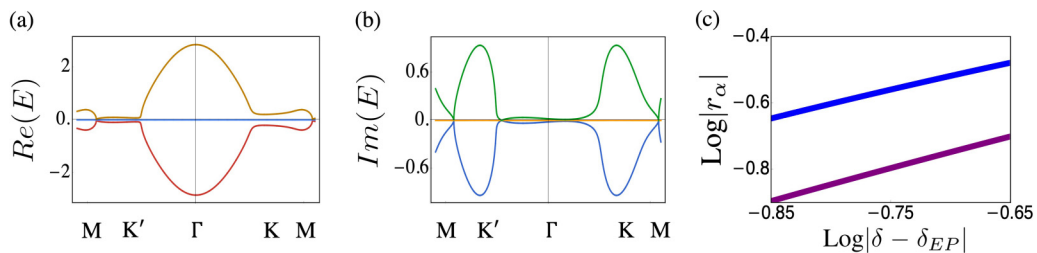


FIG. 4. Non-Hermiticity in the complete dice-Haldane lattice model. In the topologically nontrivial region $m < m^*$, non-Hermiticity strength δ induces an EP of order three close to the M point in the spectrum. Panel (a) shows the real part of the energy spectrum, panel (b) shows the imaginary part of the energy spectrum, and panel (c) shows the scaling of the phase rigidity around $\delta_{EP} = 0.94$ at $k_x = 1.07$. The different colors here correspond to different eigenstates. The r_α for the two dispersive bands overlap. Here, $t = 1/\sqrt{2}$, $t_2 = 0.06t$, $\phi = \pi/2$, and $m = 0.06$.

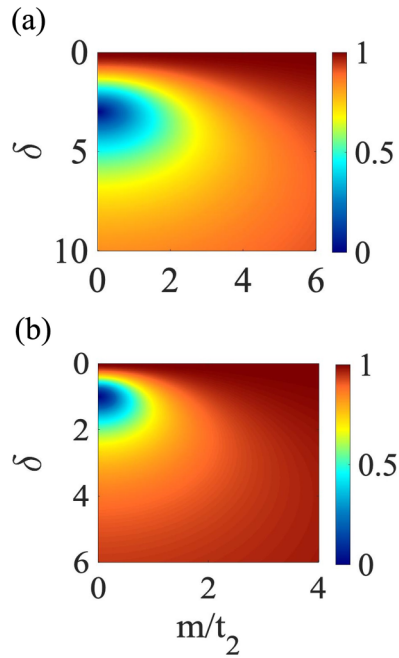


FIG. 5. Phase diagram showing the occurrence of EPs as a function of the model parameters. Panel (a) shows the phase rigidity at the Γ point while panel (b) corresponds to the M point. Zero values of phase rigidity imply the existence of third-order EPs, at the corresponding parameter values. Note the extended region in the parameter space with phase rigidity values very close to zero. Here, $t = 1/\sqrt{2}$ and $\phi = \pi/2$.

through a third-order EP. On the other hand, if we choose the value of mass m outside the topologically nontrivial region of the Hermitian case, there is no possible value of δ that will manifest in protected edge states and will trace the system back into the topological region. In other words, to obtain EPs at any finite, nonzero value of δ , we require the Hermitian system to be placed initially within the topological region. Tuning δ can bring about a topological phase transition enabling the occurrence of EPs in the non-Hermitian model.

Now, we will invoke a different class of non-Hermiticity—nonreciprocal hopping along one direction. In particular, we have assigned $t + \gamma$ ($t - \gamma$) to the hopping parameters $C \rightarrow B$ ($B \rightarrow C$) and $B \rightarrow A$ ($A \rightarrow B$) in the vertical direction in Fig. 1(a). Even in the absence of the non-Hermitian gain and loss we observe that nonreciprocal hopping solely can induce EPs in the system at specific strengths of non-Hermiticity γ . The deformation of the electronic bands under this nonreciprocity is qualitatively similar to our previous results with non-Hermitian gain and loss. However, the critical values of γ at which the EPs occur differ from the critical δ we found in the above discussion. For example, in the case with only nearest-neighbor hopping EPs are induced at critical γ values of

$$\gamma_{EP} = \pm \sqrt{\frac{3}{2} + 2 \cos(\pi k_x) + \cos(2\pi k_x)}. \quad (7)$$

Therefore, from Eq. (6) it is clear that γ_{EP} values are related to the corresponding δ_{EP} values by the relation $\gamma_{EP} = \delta_{EP}/\sqrt{2}$. Numerically, we have verified the occurrence of EP3 at $\gamma_{EP} = \pm \frac{3}{\sqrt{2}}$ and $\gamma_{EP} = \pm \frac{1}{\sqrt{2}}$ for the Γ and M points,

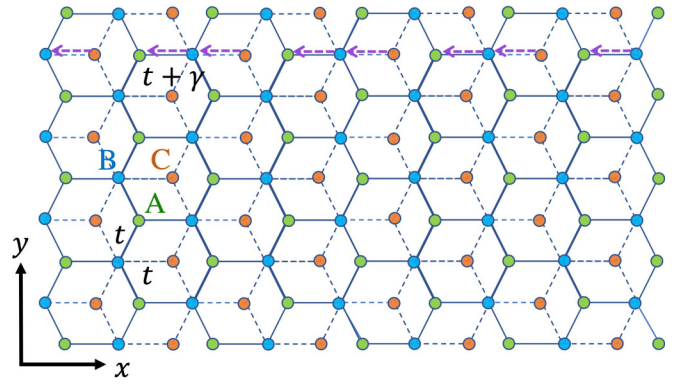


FIG. 6. Schematic of the dice-Haldane nanoribbon with nonreciprocal hopping. The hopping and on-site parameters remain the same as in the dice-Haldane sheet case. An additional kind of non-Hermiticity γ has been introduced in the nanoribbon, namely a nonreciprocal hopping. This favors nearest-neighbor hopping from right to left along the x direction rather than from left to right.

respectively. It is interesting to study this nonreciprocal hopping in the context of the dice-Haldane nanoribbon to see the effects of OBC (see Sec. IV B).

IV. FINITE-SIZE EFFECTS: DICE-HALDANE NANORIBBON

Having understood the effect of non-Hermiticity in the k -space model of the dice lattice sheet, we next move on to the study of another physically important case of the dice-Haldane nanoribbon extended along one direction (say x). A schematic of the finite-size nanoribbon considered here is shown in Fig. 6. Here L_x and L_y are the dimensions in the x and y directions, respectively. We particularly focus on a real-space model of the nanoribbon, where both L_x and L_y are finite. The real-space model with open-boundary conditions in both directions leads to interesting consequences when we invoke non-Hermiticity, as we will discuss shortly.

Considering the Hermitian model, we can expect that in the topologically nontrivial phase, each edge of the lattice will exhibit two chiral edge states since the Chern number is ± 2 . These edge modes lie in the band gap and connect two bulk bands. In contrast with the honeycomb lattice, the spectrum exhibits two unidirectional chiral states per edge for $m < m^*$ that cross over from the bulk states near the Fermi level. However, for $m > m^*$, the edge states near the flat band are counterpropagating at a given edge. Hence, no net current will flow through it. Consequently, the bulk states remain gapped out, and the bulk boundary correspondence continues to hold. Corresponding figures and a discussion can be found in Appendix C.

It is important to note that these edge states are quite robust to both real and complex on-site disorder, i.e., despite some disorder-induced distortion in the shape of the bands, the edge states persist up to large values of disorder. We have checked this for a disorder of the form Δ_j on each lattice site, where Δ_j is allowed to be real or imaginary, corresponding to real and imaginary on-site disorder, respectively. Here, j

denotes the lattice site and $\Delta_j = \Delta\omega_j$ where $\omega_j \in [-1, 1]$. The disordered Hamiltonian has the form $H = H_{nm} + H_{nmn} + H_m + H_{dis}$, where

$$H_{dis} = \sum_j \Delta_j c_j^\dagger c_j. \quad (8)$$

We study the effect of this complex random on-site disorder in more detail when we introduce non-Hermiticity in the finite-nanoribbon geometry. We address the interplay of non-Hermiticity and disorder in Sec. IV B.

A. Nanoribbon with non-Hermitian gain and loss

We first consider the effect of non-Hermitian balanced gain and loss in the dice-Haldane nanoribbon. The Hamiltonian under such considerations is given by $H = H_{nm} + H_{nmn} + H_m + H_\delta$. It is worth noting that the topological edge states found in the Hermitian regime, forming conducting channels between the conduction and valence bands are robust even in the presence of non-Hermiticity. For a range of increasing values of δ , up to a system dependent critical value δ_c , the topological edge states can be clearly discerned from the energy-band diagram. A detailed discussion can be found in Appendix C.

One of the striking features of non-Hermitian systems has been the discovery of NHSE and it is interesting to understand whether our proposed system exhibits this feature. It may be noted that these fascinating phenomena unique to non-Hermitian systems, such as non-Bloch EPs and skin effects, can be well explained in terms of the generalized Brillouin-zone (GBZ) formalism [66,103]. We note that it has been established that a two-dimensional system under OBC can exhibit NHSE if and only if under PBC the complex eigenspectrum encloses a finite nonzero spectral area [104]. We consider a periodic version of the system, i.e., a dice-Haldane torus and invoke balanced gain and loss. When we consider only nearest-neighbor interactions under PBC, the complex eigenspectrum of the system has an arc-like structure and does not enclose any finite spectral area in the complex plane, as shown in Fig. 7(a). This indicates the absence of a NHSE when we invoke OBC. To probe this, we calculate the local density of states (LDOS) for the system under OBC, i.e., the finite nanoribbon. To calculate the LDOS, we evaluate $\sum_\alpha |\psi_\alpha(x_i)|^2$ at each lattice site (x_i), which gives us $\text{LDOS}(x_i)$. The plot of the corresponding LDOS for the nearest-neighbor lattice in Fig. 7(c) verifies that NHSE is indeed absent and the states are distributed over the lattice. However, when we consider the full dice-Haldane periodic system ($t_2 \neq 0$) with balanced gain and loss, the complex spectrum does enclose a finite area [shown in Fig. 7(b)]. This translates to the occurrence of NHSE when OBC is invoked. Remarkably, the localization of the eigenstates occurs at both the top and bottom edges of the nanoribbon which can be seen from the plot of the LDOS in Fig. 7(d). So, non-Hermitian gain and loss is able to cause a NHSE in the dice-Haldane model and not in the dice model which accounts for only nearest-neighbor hopping. The nature of the skin effect occurring only at the top and bottom edges of the former system [as shown in Fig. 7(d)], can be explained further through the winding number and the complex energy spectra by imposing OBC in one direction while retaining PBC in the other. A

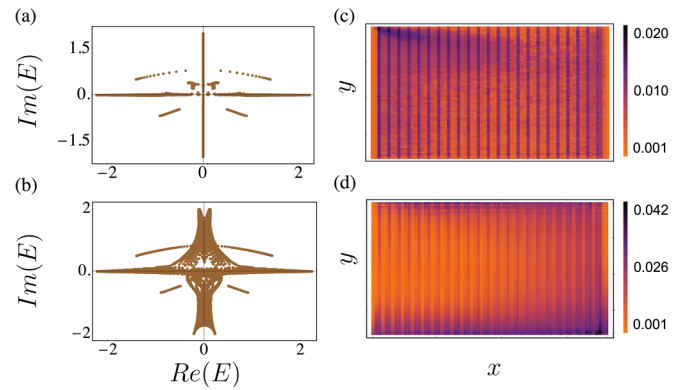


FIG. 7. Spectra and LDOS with non-Hermitian balanced gain and loss. Panels (a) and (b) show the complex energy spectrum for the torus (PBC) geometry of the nanoribbon and panels (c) and (d) show the respective LDOS for the same system under OBC. Panels (a) and (c) correspond to the nearest-neighbor lattice ($t_2 = 0$) with non-Hermitian balanced gain and loss. The energy spectrum in panel (a) does not enclose a finite, nonzero area. This implies that, under OBC, there will be no occurrence of NHSE. The corresponding LDOS of the system under OBC shown in panel (c) demonstrates the absence of skin effect. Panels (b) and (d) correspond to the full dice-Haldane lattice with gain and loss. Here, $t_2 = 0.06t$. The spectrum shown in panel (b) encloses a finite nonzero spectral area indicating the possibility of a NHSE under OBC, which is established by the LDOS shown in panel (d). In this case, the localization of states occur at both the top and bottom edges of the nanoribbon. Here, $t = 1/\sqrt{2}$, $\phi = \pi/2$, $m = 0$ and gain and loss strength $\delta = 2.0$.

detailed discussion and corresponding figures can be found in Appendix D. For all cases of our computations, the nanoribbon has 72×36 sites ($n = 2592$), unless stated otherwise.

B. Nanoribbon with nonreciprocal hopping

As we analyzed previously for the periodic dice-Haldane sheet, in this section, we consider its nanoribbon version and study the effect of nonreciprocal hopping. In particular, nonreciprocal nearest-neighbor hopping is introduced only along the x direction. We have the hopping values $t - \gamma$ along $+x$ and $t + \gamma$ along $-x$ directions, i.e., we have a biased hopping strength that favors hopping from right to left rather than from left to right. We invoke this nonreciprocal hopping throughout the bulk of the nanoribbon (see Fig. 6). We study the spectrum and LDOS of the system with this type of non-Hermiticity and find strikingly different behavior than in the case of balanced gain and loss. Unlike in the prior case, when we introduce a nonreciprocal hopping, i.e., $\gamma \neq 0$, the PBC spectrum covers a finite area in the complex plane even in case of the model with $t_2 = 0$, which implies a NHSE under OBC. In fact, the effect of nonreciprocal hopping on the nearest-neighbor model is qualitatively the same as its effect on the dice-Haldane lattice. We study the latter in detail and also discuss the effect of disorder for this case. The spectrum of the dice-Haldane model under PBC with nonreciprocal hopping accommodates a finite spectral area in the complex plane shown in Fig. 8(a). This indicates the possibility of a NHSE when we impose OBC in the system. Next, we investigate the effect of disorder on this spectral area where the nature of disorder has been taken

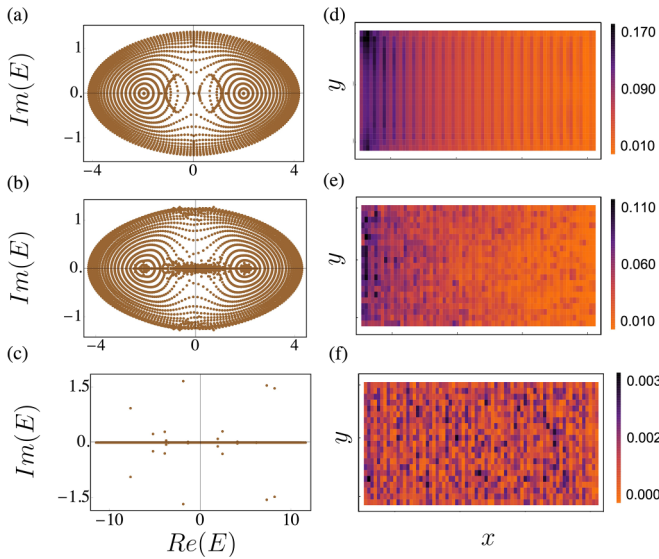


FIG. 8. Effect of disorder on the spectra and LDOS for the dice-Haldane lattice with nonreciprocal hopping. Panels (a)–(c) show the complex spectra of the model under PBC with nonreciprocal hopping. Panels (d)–(f) show the corresponding LDOS for the same system under OBC. Panels (a) and (d) show the disorder-free system. Here, the complex eigenspectrum [shown in panel (a)] encloses a nonzero spectral area which translates to a skin effect under OBC. The corresponding LDOS [shown in panel (d)] depicts a NHSE, with states accumulating close to $x = 1$, which gradually decreases as we move rightward. Panels (b) and (e) correspond to disorder strength $\Delta = 1$. Here, the spectral area [shown in panel (b)] is still nonzero and finite, implying an existence of NHSE, which is established by the LDOS in panel (e). For panels (c) and (f) where $\Delta = 10$, the spectral area has disappeared indicating the destruction of NHSE. The corresponding LDOS shown in panel (f) attributes to the same where the skin effect has completely disappeared due to localization in the bulk. Here, $t = 1/\sqrt{2}$, $t_2 = 0.06t$, $\phi = \pi/2$, $m = 0$ and nonreciprocity strength $\gamma = 2.0$.

according to Eq. (8). When the disorder strength is taken to be $\Delta = 1$, the complex spectrum undergoes some distortion but still accommodates a finite area [Fig. 8(b)]. However, at the large disorder strength ($\Delta = 10$) shown in Fig. 8(c) the spectral area disappears. This indicates that, under OBC, the NHSE will gradually get destroyed due to the introduction of disorder. Next, we investigate the behavior of the LDOS to verify the above findings and to visualize the occurrence and subsequent disappearance of the NHSE under disorder.

In Fig. 8(d) the LDOS can be seen to be higher around small values of x and decreases as we go to higher x . This implies a maximal concentration of eigenstates near the left edge of the system. Thus, nonreciprocal hopping, when invoked throughout the bulk of the nanoribbon, causes a NHSE. It is important to note that the NHSE in this case is different from that caused by gain and loss. Here, the localization of the eigenstates is at one edge (left) of the lattice and is also directionally different than in the previous case where NHSE occurred at the top and bottom edges. In the former case of gain and loss, the inclusion of the Haldane next-nearest neighbor hopping is essential for realizing the skin effect. Here, the staggered magnetic flux in the presence of non-Hermitian

gain and loss introduces chiral edge currents in two different directions for the two distinct sublattices A and C [105]. Consequently, the eigenmodes are localized at the top and bottom edges of the ribbon under OBC. In contrast, the nonreciprocal hopping along one direction offers a directionally biased propagation of eigenstates, causing localization at the left edge. We find that the LDOS does not vary continuously from high to low as we move along $+x$ but shows regions of high value followed by those of lower value. This feature is due to the missing hopping terms between sublattices A and C, which inhibits the complete flow of the eigenstates leftwards. This can be pictured from the schematic in Fig. 6, which suggests that the accumulation of states will be greater on sublattice C and gradually decrease towards the following A lattice site. Now, we look at the effect of disorder on the NHSE. Upon increasing the value of disorder strength, there occurs a localization of the eigenstates, as shown in Figs. 8(e) and 8(f). In Fig. 8(e) corresponding to $\Delta = 1$ the concentration of eigenstates at the left edge has decreased, signifying a partial destruction of the NHSE. Finally, at large values of disorder ($\Delta = 10$), a complete localization of the eigenfunctions is found, causing a low value of the LDOS over all x , implying the complete destruction of the NHSE [Fig. 8(f)].

To consolidate the above arguments, we next study the behavior of the IPR [86] and the probability density of the eigenstates at the edge after averaging both the quantities over multiple disorder configurations. We averaged over 1000 disorder configurations. The IPR for the α th eigenstate, I_α , is defined as

$$I_\alpha = \frac{\sum_r |\psi_\alpha(r)|^4}{(\sum_r |\psi_\alpha(r)|^2)^2}. \quad (9)$$

For localized states, IPR is close to 1 while for extended states IPR is very low. We further define the edge probability, P_α , of state ψ_α as

$$P_\alpha = \frac{\sum_{x_i=1}^{x_E} |\psi_\alpha(x_i)|^2}{\sum_{x_i} |\psi_\alpha(x_i)|^2}, \quad (10)$$

where x_E represents the width of the edge, which we take as the first five lattice sites from the left end of the ribbon ($x_E = 5$). In the case of the Hermitian nanoribbon the dispersive bands are delocalized with very low IPR and there is no skin effect as expected. In presence of nonreciprocity in the bulk ($\gamma = 2$) we observe $\text{IPR} \rightarrow 1$ for the eigenstates localized at the edge. This can be seen from Fig. 9(a) where the edge probability is denoted by the color bar showing that the states with high P_α correspond to high IPR. Hence, for the disorder-free case with nonreciprocal bulk we can confirm the occurrence of NHSE. Next, we look at the effect of disorder on the skin effect—the presence of disorder essentially reduces the edge localization in the system. This can be discerned from the diminished values of the IPR in Fig. 9(b), presented for disorder strength $\Delta = 1$. Yet, the higher values of IPR are predominantly contributed by the eigenstates near the edge. Furthermore, for large disorder strength ($\Delta = 10$), shown in Fig. 9(c), the IPR is uniformly high, although P_α is very low for all the eigenstates. This corresponds to the disorder induced bulk localization and hence the complete destruction of NHSE.

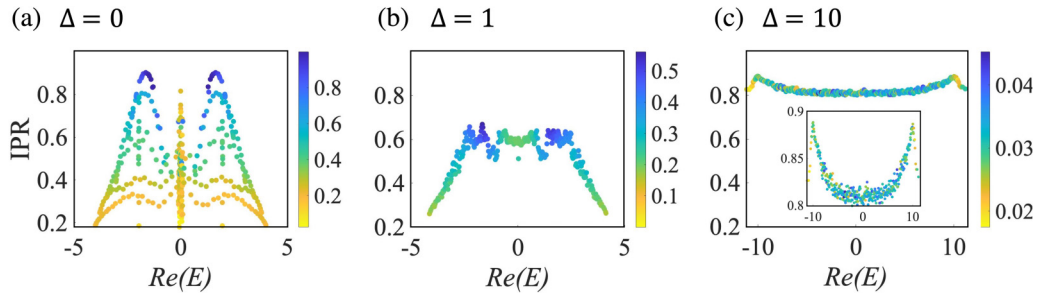


FIG. 9. IPR and edge probability with nonreciprocal bulk. The IPR has been plotted for all eigenstates as a function of $\text{Re}(E)$ and the corresponding color denotes its probability density at the left edge of the nanoribbon. Panel (a) corresponds to $\Delta = 0$, where the IPR is very high for the states localized at the edge and hence establishes the occurrence of NHSE. In panel (b) the IPR values have diminished, implying the reduction of skin effect due to disorder. Here, disorder strength $\Delta = 1$. Panel (c), corresponding to $\Delta = 10$, shows very high values of IPR but very low edge population implying the occurrence of disorder-induced bulk localization and complete destruction of NHSE. A zoomed-in plot is shown in the inset. Here, the IPR and edge probability have been disorder averaged over 1000 configurations. The number of hexagonal layers in the y direction has been taken to be 35. We have set $t = 1/\sqrt{2}$, $t_2 = 0.06t$, $\phi = \pi/2$, $m = 0$, $\delta = 0$, $\gamma = 2$.

Finally, we also note that when we invoke nonreciprocal hopping only along the upper and lower edges of the system and not in the bulk, surprisingly, here too there is the occurrence of the NHSE which is similarly destroyed at large values of disorder.

V. SUMMARY AND DISCUSSION

In this work, we have systematically studied the effect of non-Hermiticity in the Chern insulating dice-Haldane lattice.

We introduced non-Hermiticity in this model in two ways: (i) using balanced gain and loss terms and (ii) setting nonreciprocal hopping parameters. Introducing non-Hermiticity through any of the above means invariably causes higher-order exceptional points. Our analytical description revealed that the exceptional points at high-symmetry points emerge at odd integer values of the gain and loss non-Hermiticity strength and at $1/\sqrt{2}$ times the previous values in the case of nonreciprocal hopping. Furthermore, we showed that the dice-Haldane lattice consisting of complex next-nearest-neighbor hopping and the Semenoff mass offers a rich topological phase diagram. The robustness of the topological edge states was critically examined with non-Hermiticity and complex disorder. Moreover, we discover that, unlike the gain and loss case, the nonreciprocal hopping triggers a fascinating non-Hermitian skin effect under OBC for the dice lattice with only nearest-neighbor couplings. However, both kinds of non-Hermiticity can cause NHSE in the more general dice-Haldane nanoribbon. Remarkably, the NHSE caused by gain and loss generates localization at the top and bottom edges while nonreciprocity results in a NHSE at the left edge of the nanoribbon. The directionality of localization of maximal eigenstates can hence be tuned using the nature of non-Hermiticity and its strength. The skin effect is protected by a finite spectral area in the complex plane under PBC in real space. Furthermore, the LDOS, IPR, and edge probability calculations also demonstrate the occurrence of the skin effect and its robustness to the disorder.

Our study is fundamental to understanding the tunability of the dice-Haldane model under the influence of non-Hermiticity, especially in the context of EPs which have been experimentally realized in microwave cavity resonators [59]

and coupled electronic circuits [106]. Specifically, EPs of order three have been realized in coupled acoustic cavity resonators [107] and optical cavity systems [61]. It would be interesting to engineer already fabricated dice lattices to introduce non-Hermitian gain and loss or nonreciprocal hopping to obtain these higher-order EPs.

The key ingredients for attaining a dice lattice in cold atomic systems are three pairs of counterpropagating lasers placed at an angle of 120° with respect to each other [14,16]. This laser setup essentially divides the two-dimensional (2D) plane into six equivalent parts. Furthermore, the interference causes standing waves that give rise to the required potential traps of the optical lattice. In particular, a dice lattice with lattice constant a_0 can be constructed by using six linearly polarized laser beams of wavelength $\lambda = 3a_0/2$. Another plausible pathway for fabricating these lattices is the use of coupled resonators [17]. The prescription is the incorporation of additional resonators at the center of hexagonal rings of the honeycomb lattice. The ring-shaped primary resonators of the lattice are effectively connected with each other via auxiliary resonators placed in between. The Haldane model has been experimentally realized in optical lattices using ultracold atoms [10]. Notably, the time-reversal symmetry can be broken through complex next-nearest-neighbor tunneling induced by circular modulation of the lattice position in time. Additionally, the deformation of lattice geometry by applying unidirectional in-plane force with the help of a magnetic-field gradient provides an energy offset and breaks the inversion symmetry.

Non-Hermiticity has been successfully engineered into several optical lattices, acoustic systems and topoelectrical circuits [101,107–109]. In particular, the inclusion of non-Hermiticity in the three-site Lieb lattice using coupled optical waveguides [110] can be feasibly extended to our lattice system. It has been established that optical lattices fabricated using femtosecond-direct-laser-writing can adduce non-Hermitian gain and loss through periodic “breaks” in the waveguides, which lead to loss of radiation modes. This loss can be tuned using the length of the breaks [111]. This method of engineering gain and loss has also been successfully realized in a graphene-like honeycomb lattice [112]. Furthermore, it has been proposed that atomic loss in ultracold

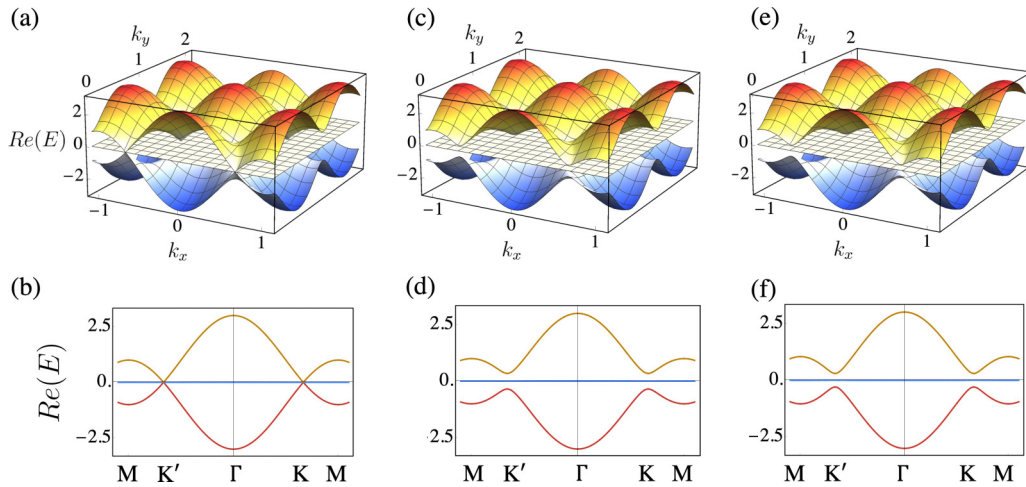


FIG. 10. Energy spectra of the Hermitian model. The band structure of the Hermitian dice-Haldane model along high-symmetry points M - K' - Γ - K - M . The upper panels show the three-dimensional spectrum as a function of k_x and k_y , while the lower panels show the corresponding two-dimensional plots at $k_y = 0$. Panels (a) and (b) show the effect of only nearest-neighbor hopping with $t_2 = m = 0$. Here, all three bands are gapless at the K and K' points. In panels (c) and (d) next-nearest-neighbor hopping has been included. Here, $t_2 = 0.1$, $\phi = \pi/2$ while $m = 0$. In panels (e) and (f) $m = 0.3$ while $t_2 = 0$ shows the effect of the Semenoff mass term. Both t_2 and m open up a gap in the spectrum. For all plots the value of nearest neighbor hopping is chosen to be $t = 1/\sqrt{2}$.

atomic gas systems can be generated using a resonant optical beam to kick the weakly trapped atoms or by using a radio frequency to excite the atom to an irrelevant state, thereby simulating loss [113]. Onsite gain and loss can be effectively mapped onto a non-Hermiticity-controlled coupling between neighboring atoms. A synthetic imaginary gauge field engineered strategically can make these couplings asymmetric [114]. Such complex gauge potentials causing nonreciprocal hopping can be implemented using a non-Hermitian antiresonance ring [57]. Due to the directional coupling, the photons become attenuated or amplified depending on their direction of travel. Furthermore, two-dimensional non-Hermitian systems with gain and loss or nonreciprocity have been proposed in classical topoelectrical circuits [108,109], where the non-Hermiticity can be ingeniously engineered using combinations of resistances and LC-tanks. Information about the eigenenergies can be extracted from the electrical response, admittance, and impedance resonances [115]. In light of the above rapid experimental advances, we believe our theoretical findings can be experimentally tested in the near future.

ACKNOWLEDGMENTS

R.S. acknowledges Indian Institute of Science for financial support. A.B. thanks the IoE postdoctoral fellowship for support. R.S. and A.B. would also like to thank A. Banerjee for several useful discussions. A.N. acknowledges support from the start-up grant (SG/MHRD-19-0001) of the Indian Institute of Science and DST-SERB (Project No. SRG/2020/000153).

APPENDIX A: HERMITIAN DICE-HALDANE BAND DIAGRAMS

We perform a Fourier transform of the Hamiltonian given in Eqs. (1) and (2) in order to obtain the energy-band diagram

in the two-dimensional momentum space. To encompass all the relevant physics of the model, we choose a symmetry path $M(1, 0)$ - $K'(-2/3, 0)$ - $\Gamma(0, 0)$ - $K(2/3, 0)$ - $M(1, 0)$ in the BZ, which includes all the high-symmetry points. Note that the coordinates of the symmetry points are given in units of $2\pi/a$, where a is the lattice constant. Later, we systematically invoke non-Hermiticity in our model and study the physics around these high-symmetry points. The dice lattice with only nearest-neighbor interactions ($H_{nmn} = H_m = 0$), exhibit two Dirac-like dispersive bands while a dispersion-less flat band lies at the Fermi level, as shown in Figs. 10(a) and 10(b). The Dirac points lie at the symmetry points K and K' of the BZ. Next, the complex next-nearest-neighbor hopping term ($H_m = 0$) splits the Dirac cones as shown in Figs. 10(c) and 10(d), resulting in nontrivial topological band structures. On the contrary, only Semenoff mass term ($H_{nmn} = 0$) induces a trivial or normal band gap in the system as given in Figs. 10(e) and 10(f). It is worth noting that both H_{nmn} and H_m open up a gap in the energy spectrum even for arbitrarily small values of t_2 and m . The competing nature of H_{nmn} and H_m leads to the rich topological phase diagram of the dice-Haldane model.

In particular, Fig. 11 illustrates the effect of the Semenoff mass on the electronic band structure of the nontrivial dice-Haldane model. Even an arbitrarily small nonzero value of m opens up a band gap at the K and K' points of the BZ while maintaining topologically nontrivial features [Fig. 11(a)]. With a further increase in m , for a critical value $m = m^*$, the K' point becomes triply degenerate while the K point develops no such band touching [Fig. 11(b)]. Beyond this point, for $m > m^*$, the system becomes topologically trivial and the energy bands are completely nondegenerate for all higher values of m [Fig. 11(c)]. It is interesting that the different phases of the Hermitian model exhibit qualitatively different energy-band structures. The AG phase features three nondegenerate bands as shown in Figs. 12(a) and 12(b). The upper panel in Fig. 12 shows the three-dimensional band

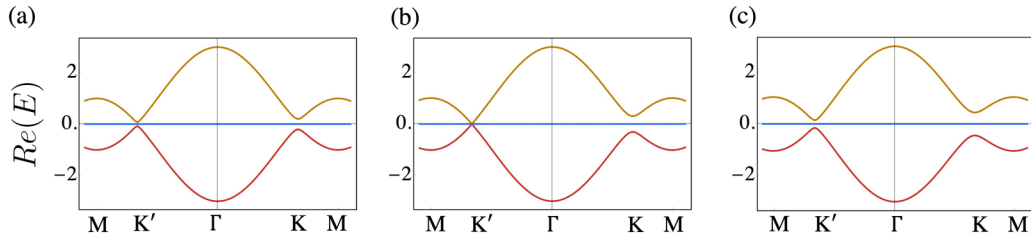


FIG. 11. Effect of the Semenoff mass in the Hermitian model with both t and t_2 . In panel (a) $m = 0.06$, in panel (b) $m = 0.16$, and in panel (c) $m = 0.30$. An arbitrarily small Semenoff mass opens up a gap in the spectrum which subsequently closes in panel (b) indicating a semimetallic phase. On increasing the value of m further, all bands become gapped again. This critical value of m is $m^* = 0.16$ which separates the topologically nontrivial and trivial regions in panels (a) and (c), respectively. For all plots $t = 1/\sqrt{2}$, $t_2 = 0.06t$, and $\phi = \pi/2$.

structure as a function of k_x and k_y , while the lower panel is a two-dimensional plot of the dispersion relations along line (M - K' - Γ - K - M) joining the high-symmetry points of the BZ. The VG phase is shown in Figs. 12(c) and 12(d) where the valence band remains gapped while the flat band and conduction band are degenerate at some points in the BZ. Figures 12(e) and 12(f) show the CG phase where the conduction band is nondegenerate while the valence and flat bands become gapless.

APPENDIX B: EFFECT OF GAIN AND LOSS IN THE DICE LATTICE MODEL

We consider the nearest-neighbor hopping in the Hamiltonian while keeping t_2 and m switched off. We introduce non-Hermiticity to the system and study its effects as we vary the strength of gain and loss, δ . In this condition, the Hamiltonian has the form $H = H_{nm} + H_\delta$, where δ is tuned methodically. The band diagram for the Hermitian case, i.e., at $\delta = 0$, has been previously shown in Fig. 10(a) and 10(b). As we invoke gain and loss, a complex dispersion relation ap-

pears even for arbitrarily small values of δ . Such a dispersion relation results in a complex eigenvalue spectrum owing to the non-Hermitian nature of the Hamiltonian. Particularly, the real part of the spectra in this condition become a single-sheeted hyperboloid around the K point, near which the imaginary part of the spectra has a nonvanishing contribution as shown in Figs. 13(a) and 13(b). Here, the appearance of complex energy spectra is exciting because the \mathcal{PT} operator still commutes with the Hamiltonian. Therefore, the only explanation is that the Hamiltonian and \mathcal{PT} symmetry operators do not possess the same set of eigenvectors underpinned by the antilinear nature of the T operator. Similar features have also been evinced for graphene in the presence of non-Hermitian gain and loss [116]. This can be explicitly shown for the dice lattice where the \hat{P} operator maps $A \leftrightarrow C$ lattice sites and is given by the following matrix:

$$\hat{P} = \begin{pmatrix} 0 & 0 & 1 \\ 0 & 1 & 0 \\ 1 & 0 & 0 \end{pmatrix}, \quad (\text{B1})$$

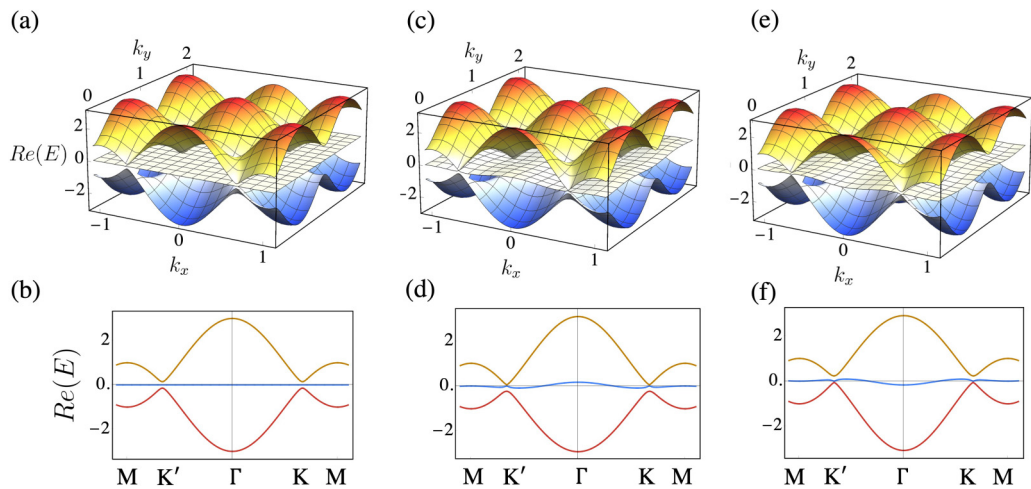


FIG. 12. Energy spectra of the different phases in the Hermitian model. The band structure of the Hermitian dice-Haldane model along high-symmetry points M - K' - Γ - K - M . The upper panels show the three-dimensional spectrum as a function of k_x and k_y , while the lower panels show the corresponding two-dimensional plots at $k_y = 0$. Panels (a) and (b) show the all-gapped (AG) phase with $\phi = \pi/2$ and $m = 0$. Here, all three bands are gapped for all values of k_x and k_y . Panels (c) and (d) show the valence-gapped (VG) phase where the conduction and flat bands are gapless while the valence band remains gapped. Here, $\phi = 0$ and $m = 0.15$. In panels (e) and (f) $m = 0.15$ and $\phi = \pi$, which shows the conduction-gapped (CG) phase, where the conduction band is gapped while the valence and the flat bands are gapless. For all plots the values of $t = 1/\sqrt{2}$ and $t_2 = 0.06t$.

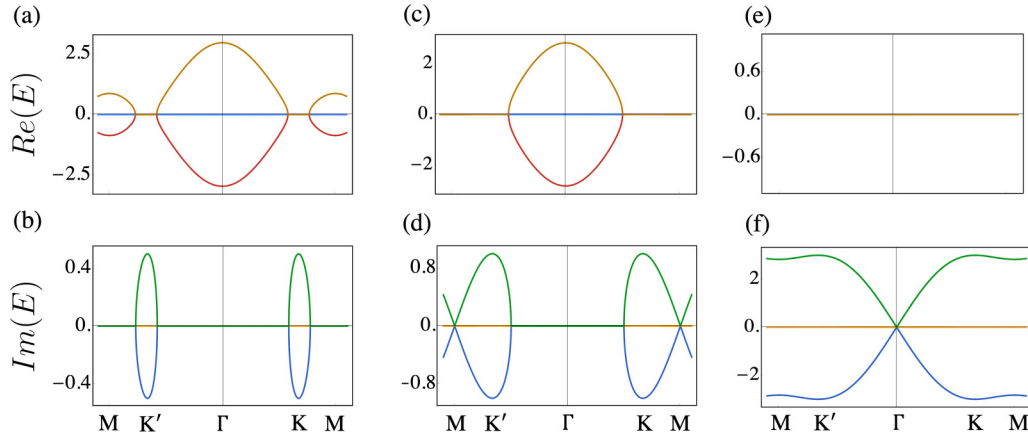


FIG. 13. Energy spectra of the model with nearest-neighbor hopping and non-Hermiticity. The $\text{Re}(E)$ (upper panels) and $\text{Im}(E)$ spectra (lower panels) have been shown for different values of non-Hermiticity strength δ . In panels (a) and (b) $\delta = 0.5$ showing that the non-Hermitian gain and loss instantly makes the K and K' points of $\text{Re}(E)$ degenerate while the degeneracy is lifted in $\text{Im}(E)$. In panels (c) and (d) $\delta = 1.0$, this induces an EP at the M point where both the $\text{Re}(E)$ and $\text{Im}(E)$ are simultaneously degenerate. Similarly in panels (e) and (f) we find an EP at the Γ point for $\delta = 3.0$. For all plots we have set $t = 1/\sqrt{2}$.

and \hat{T} is the antiunitary complex conjugation operator for our spinless system. It can be shown that the commutation relation $[\hat{P}\hat{T}, H(k)]$ is invariably zero for arbitrary values of δ . On the other hand, the eigenvectors of the $\hat{P}\hat{T}$ and H operators, particularly shown below for the Γ point, are clearly distinct:

$$\hat{P}\hat{T} \rightarrow \begin{bmatrix} -1 \\ 0 \\ 1 \end{bmatrix}, \begin{bmatrix} 1 \\ 0 \\ 1 \end{bmatrix}, \begin{bmatrix} 0 \\ 1 \\ 0 \end{bmatrix}, \quad (\text{B2})$$

$$H \rightarrow \begin{bmatrix} -1 \\ a \\ 1 \end{bmatrix}, \begin{bmatrix} a\eta_- \\ \eta_- \\ 1 \end{bmatrix}, \begin{bmatrix} a\eta_+ \\ \eta_+ \\ 1 \end{bmatrix}, \quad (\text{B3})$$

where $\eta_{\pm} = a \pm (2 + a^2)^{1/2}$ and $a = \frac{\sqrt{2}}{3}i\delta$. Hence, despite \mathcal{PT} symmetry of the system, the eigenstates correspond to the broken- \mathcal{PT} phase.

A further increase in δ extends the degeneracy of $\text{Re}(E)$ to M , while the degeneracy at this point in $\text{Im}(E)$ is lifted as presented in Figs. 13(c) and 13(d). Most interestingly, this critical transition at the M point occurs exactly at $\delta = 1.0$. At this value of δ , we find that the three eigenvalues and eigenfunctions coalesce at the M point, giving rise to a third-order EP. As we increase δ further, the branches of $\text{Re}(E)$ becomes degenerate while the degeneracy is lifted in $\text{Im}(E)$ at the corresponding k_x values. At $\delta = 3.0$, we find the coalescence of the three eigenvalues and eigenfunctions at the Γ point [Fig. 13(e) and 13(f)]. This is again a third-order EP, however, appearing at a different point in the BZ. The phase rigidity and its scaling for this EP are shown in Fig. 14. Figure 14(a) shows the variation of phase rigidity r_{α} of the eigenvectors as a function of δ . $r_{\alpha} \rightarrow 0$ as $\delta \rightarrow \delta_{EP} = 3.0$. The scaling of the phase rigidity has been plotted on a logarithmic scale in Fig. 14(b) whose slope is one, denoting that the higher-order EP is indeed of order three.

APPENDIX C: NON-HERMITICITY AND EDGE STATES IN THE DICE-HALDANE NANORIBBON

Topological zero-energy modes which are found in the nontrivial region of the Hermitian model have been shown in Fig. 15(a), characterized by the linear zero-energy crossings from the conduction to the valence band. The zero modes disappear as one moves into the topologically trivial region of the phase diagram, as shown in Fig. 15(b). Figures 15(a) and 15(b) show the spectrum close to the Fermi level ($E = 0$) along the line joining high-symmetry points: $X-\Gamma-X$.

Sitting in the topologically nontrivial region, we have studied the energy spectrum for a varying non-Hermiticity strength δ . We found that the existing edge states are robust to values of δ up to $\delta_c = 0.8$ for the energy scale of our system, after which the edge states cannot be discerned from the bulk states. This can be seen in Fig. 15(c), where we still decipher clear edge states for $\delta < \delta_c$ and subsequently the edge states disappear for $\delta > \delta_c$ [Fig. 15(d)]. Figures 15(e) and 15(f) show the imaginary spectra corresponding to Figs. 15(c) and 15(d), respectively. We can see that the spectra develops finite nonzero $\text{Im}(E)$ as a result of introducing non-Hermiticity into the nanoribbon, yet the real spectra can accommodate topological edge states up to δ_c .

It is well established that the bulk boundary correspondence in a system generally breaks down due to the presence of non-Hermiticity [42,77,117–119]. As a consequence, the Chern number of the momentum space bulk Hamiltonian fails to predict the existence of topological edge states correctly. In principle, a topological invariant may be calculated by taking into account the GBZ formalism [103]. However, for a two-dimensional, nontrivial model, it is a challenging task to deduce the GBZ. An alternative approach has been explored in Ref. [120], where a finite two-dimensional topological Haldane lattice has been constructed with arbitrary edge types. In these finite two-dimensional systems, edge states appear even if the eigenvalues are not entirely real due to the presence of gain and loss. Moreover, in this \mathcal{PT} -symmetry-broken

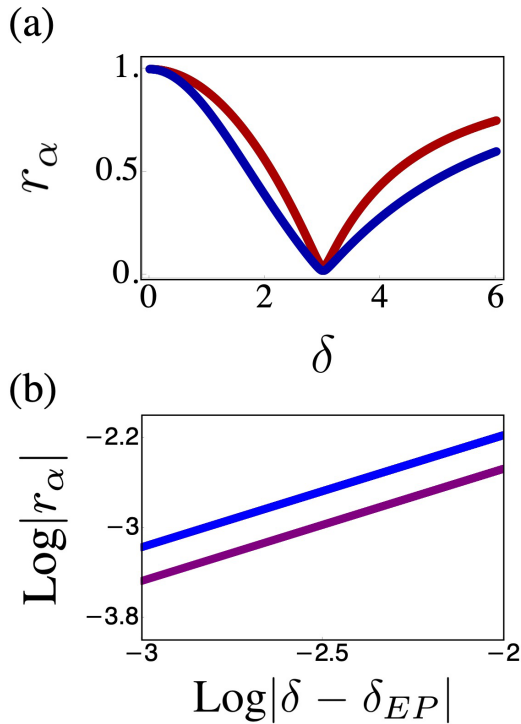


FIG. 14. Variation of phase rigidity for the model with nearest-neighbor hopping with non-Hermiticity. Panel (a) shows the phase rigidity of the eigenfunctions r_α as a function of non-Hermiticity δ , while panel (b) shows the scaling of the corresponding r_α around the concerned EP. Here, the plots have been shown for the Γ point where an EP is induced at $\delta = 3.0$. At this point, $r_\alpha \rightarrow 0$ shown in panel (a). Panel (b) shows the logarithmic scaling of r_α around $\delta_{EP} = 3.0$ gives a slope of unity implying it is an EP of order three. The different colors in both the plots correspond to different eigenstates. The r_α for the two dispersive bands overlap. For both plots we have set $t = 1/\sqrt{2}$.

phase, the topological protection has been determined by the number of edge states that remain within the dissipation- or amplification-free region. The absence of backscattering, hence the topological phase, has been confirmed by calculating the time evolution of an edge state. As expected, the number of real edge states essentially depends on the strength of gain and loss (δ), which drives the topological transition. We have used a similar formalism for our model to calculate the critical values of δ (δ_c) corresponding to the topological protection. The numerical value of δ_c has been obtained from the maximum value of gain or loss for which at least 5% of the edge states remain dissipation- or amplification-free. We note that the value of δ_c for the dice-Haldane system varies with system size similar to the conventional Haldane model. For example, $\delta_c = 0.8$ for a smaller lattice size, say $n = 288$. However, for the system with sufficiently large number of lattice sites (checked for $n = 1152$ and $n = 5220$), the critical value of δ_c saturates to ≈ 1 as depicted in the Fig. 16. Figures 15(c) and 15(d) illustrate the effect of gain and loss strength on the real part of the nanoribbon band structure in momentum space. Here, under the time-reversal symmetry broken condition, the Semenoff mass term is chosen as $m = 0.06$, ensuring the nontrivial topological phase of the

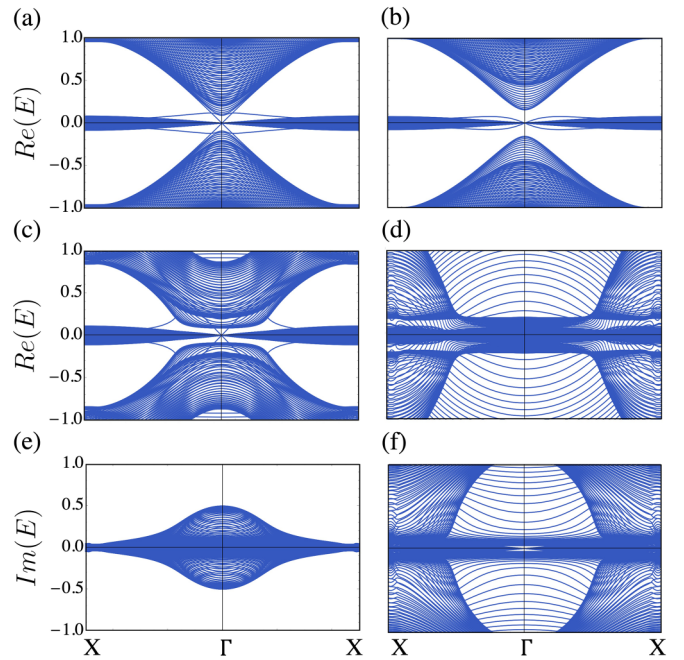


FIG. 15. Effect of gain and loss on the edge states of the nanoribbon. Here, the nanoribbon has been considered to be finite in the y direction while we have imposed PBC along x . Panels (a) and (b) correspond to the Hermitian nanoribbon. Panel (a) shows the real spectrum for $m = 0.06$ and panel (b) shows the spectrum for $m = 0.3$. The spectra have been plotted along high-symmetry lines $X-\Gamma-X$. In the topologically nontrivial region we find conducting edge states in the spectrum [shown in panel (a)], while in the topologically trivial region [shown in panel (b)] no nontrivial edge states are present. Panels (c) and (d) show the persistence of edge states in the nanoribbon with non-Hermitian gain and loss while in the topologically nontrivial region ($m = 0.06$). The edge states are robust to δ up to a critical value of $\delta_c \approx 1$, after which they disappear. (c) The presence of edge states in the real energy spectra can be seen for $\delta = 0.5 < \delta_c$. (d) The edge state is absent for $\delta = 1.5 > \delta_c$, as expected. The corresponding imaginary spectra for panels (c) and (d) have been shown in panels (e) and (f), respectively. The system with non-Hermiticity has a finite nonzero $\text{Im}(E)$ yet the real part of the spectra can still accommodate edge states. Here, the number of hexagonal layers in the y direction has been taken to be 70. We have chosen $t = 1/\sqrt{2}$, $t_2 = 0.06t$, and $\phi = \pi/2$.

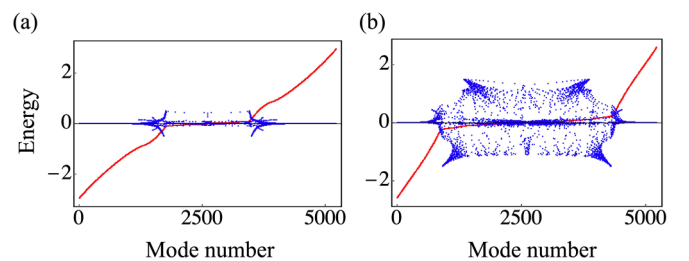


FIG. 16. Real and imaginary parts of energy for the dice-Haldane nanoribbon with gain and loss. $\text{Re}(E)$ is shown in red and $\text{Im}(E)$ is shown in blue. Panel (a) shows $\text{Re}(E)$ and $\text{Im}(E)$ for gain and loss strength $\delta = 0.5$. Panel (b) corresponds to $\delta = 1.5$. The other parameters for the plots are $t = 1/\sqrt{2}$, $t_2 = 0.06t$, $m = 0.0$, and $\phi = \pi/2$. The total number of lattice sites $n = 5220$. The number of edge states that remain in the dissipation- or amplification-free region is reduced with increasing gain and loss strength.

Hermitian system to start with. We observed that the non-Hermiticity in terms of gain and loss above the critical value essentially destroys the topologically protected edge states in the lattice.

APPENDIX D: GEOMETRY-DEPENDENT SKIN EFFECT UNDER NON-HERMITIAN GAIN AND LOSS

The finite spectral area of the dice-Haldane torus (PBC in both directions) in the complex plane cannot solely explain the appearance of skin effect only on the top and bottom edges. The nature of skin effect shown in Figs. 7(b) and 7(d) under non-Hermitian gain and loss resembles the geometry-dependent skin effect mentioned in Ref. [104]. To illustrate, we calculate the Zak phase [121] and the corresponding winding number (W) of the filled bands [122] along different directions, supporting our findings of the skin effect. Additionally, we elucidate how the complex energy spectrum can also be used to predict NHSE in the top and bottom edges (y direction) in Figs. 7(b) and 7(d) rather than along the length (x direction), which can occur on imposing nonreciprocal hopping [Fig. 8]. For that purpose, we consider the following two cases

Case 1. We impose PBC along the y direction while we have OBC along x . The energy spectrum in the complex plane of this nanoribbon under gain and loss shows a loop-like structure enclosing a finite spectral area. This implies a skin effect when OBC is imposed along the y direction, i.e., along the top and bottom edges of the sheet. To confirm this observation, we have calculated the Zak phase and the corresponding winding number. We find that the filled bands contribute to $W = 1$ [see Fig. 17(a)] as per expectation.

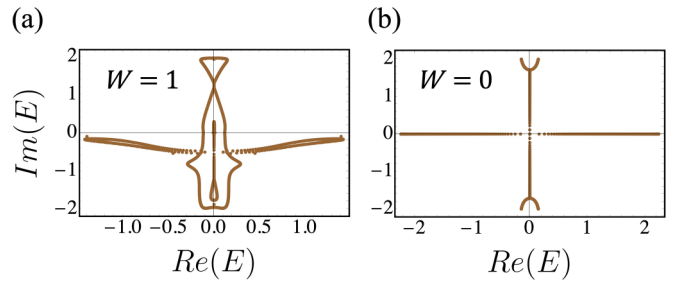


FIG. 17. Complex energy spectra and winding number under gain and loss in the dice-Haldane ribbon under two different orientations. Panel (a) shows the complex energy spectrum of the ribbon with PBC along y and OBC along x . The spectrum encloses a finite spectral area which implies the existence of a skin effect in the y direction when one imposes OBC. The skin effect has been confirmed by the winding number, $W = 1$. Panel (b) shows the complex energy spectrum of the ribbon with PBC along x and OBC along y . The spectrum shows an arc-like structure with no enclosed area. This signifies that no skin effect will occur along the x direction when OBC is imposed. The absence of skin effect in this case has been confirmed by the winding number, $W = 0$. For the above plots the values of $t = 1/\sqrt{2}$, $t_2 = 0.06t$, $m = 0$, $\delta = 2.0$, and $\phi = \pi/2$.

Case 2. We consider the ribbon to be periodic in the x direction and open along y . The spectrum in this case has an arc-like structure in the complex plane, which does not enclose a finite spectral area. This implies that on imposing OBC in the x direction, skin effect will not occur at the right or left edges. In this geometry we find $W = 0$ for the filled bands [see Fig. 17(b)].

-
- [1] S. Sachdev, *Quantum Phase Transitions*, 2nd ed. (Cambridge University Press, 2011).
- [2] K. v. Klitzing, G. Dorda, and M. Pepper, *Phys. Rev. Lett.* **45**, 494 (1980).
- [3] F. D. M. Haldane, *Phys. Rev. Lett.* **61**, 2015 (1988).
- [4] D. N. Sheng, Z. Y. Weng, L. Sheng, and F. D. M. Haldane, *Phys. Rev. Lett.* **97**, 036808 (2006).
- [5] T. Thonhauser and D. Vanderbilt, *Phys. Rev. B* **74**, 235111 (2006).
- [6] N. Hao, P. Zhang, Z. Wang, W. Zhang, and Y. Wang, *Phys. Rev. B* **78**, 075438 (2008).
- [7] E. J. Bergholtz and Z. Liu, *Int. J. Mod. Phys. B* **27**, 1330017 (2013).
- [8] F. D. M. Haldane, *Rev. Mod. Phys.* **89**, 040502 (2017).
- [9] G. W. Semenoff, *Phys. Rev. Lett.* **53**, 2449 (1984).
- [10] G. Jotzu, M. Messer, R. Desbuquois, M. Lebrat, T. Uehlinger, D. Greif, and T. Esslinger, *Nature (London)* **515**, 237 (2014).
- [11] B. Sutherland, *Phys. Rev. B* **34**, 5208 (1986).
- [12] J. Vidal, R. Mosseri, and B. Douçot, *Phys. Rev. Lett.* **81**, 5888 (1998).
- [13] J. Vidal, P. Butaud, B. Douçot, and R. Mosseri, *Phys. Rev. B* **64**, 155306 (2001).
- [14] D. Bercioux, D. F. Urban, H. Grabert, and W. Häusler, *Phys. Rev. A* **80**, 063603 (2009).
- [15] F. Wang and Y. Ran, *Phys. Rev. B* **84**, 241103(R) (2011).
- [16] G. Möller and N. R. Cooper, *Phys. Rev. Lett.* **108**, 045306 (2012).
- [17] S. M. Zhang and L. Jin, *Phys. Rev. B* **102**, 054301 (2020).
- [18] S. Cheng, H. Yin, Z. Lu, C. He, P. Wang, and G. Xianlong, *Phys. Rev. A* **101**, 043620 (2020).
- [19] X.-H. Wang, J. J. Wang, J. Wang, and J.-F. Liu, *Phys. Rev. B* **103**, 195442 (2021).
- [20] A. Iurov, L. Zhemchuzhna, G. Gumbs, D. Huang, and P. Fekete, *Phys. Rev. B* **105**, 115309 (2022).
- [21] S. Mukherjee, A. Spracklen, D. Choudhury, N. Goldman, P. Öhberg, E. Andersson, and R. R. Thomson, *Phys. Rev. Lett.* **114**, 245504 (2015).
- [22] R. A. Vicencio, C. Cantillano, L. Morales-Inostroza, B. Real, C. Mejía-Cortés, S. Weimann, A. Szameit, and M. I. Molina, *Phys. Rev. Lett.* **114**, 245503 (2015).
- [23] Y. Zong, S. Xia, L. Tang, D. Song, Y. Hu, Y. Pei, J. Su, Y. Li, and Z. Chen, *Opt. Express* **24**, 8877 (2016).
- [24] S. Mukherjee, M. Di Liberto, P. Öhberg, R. R. Thomson, and N. Goldman, *Phys. Rev. Lett.* **121**, 075502 (2018).
- [25] T. Andrijauskas, E. Anisimovas, M. Račiūnas, A. Mekys, V. Kudriašov, I. B. Spielman, and G. Juzeliūnas, *Phys. Rev. A* **92**, 033617 (2015).

- [26] B. Dey, P. Kapri, O. Pal, and T. K. Ghosh, *Phys. Rev. B* **101**, 235406 (2020).
- [27] Y. Ashida, Z. Gong, and M. Ueda, *Adv. Phys.* **69**, 249 (2020).
- [28] R. El-Ganainy, K. G. Makris, M. Khajavikhan, Z. H. Musslimani, S. Rotter, and D. N. Christodoulides, *Nat. Phys.* **14**, 11 (2018).
- [29] K. Kawabata, K. Shiozaki, M. Ueda, and M. Sato, *Phys. Rev. X* **9**, 041015 (2019).
- [30] I. Rotter, *J. Phys. A: Math. Theor.* **42**, 153001 (2009).
- [31] V. Martinez Alvarez, J. Barrios Vargas, M. Berdakin, and L. Foa Torres, *Eur. Phys. J. Spec. Top.* **227**, 1295 (2018).
- [32] C. M. Bender, *Rep. Prog. Phys.* **70**, 947 (2007).
- [33] A. Ghatak and T. Das, *J. Phys.: Condens. Matter* **31**, 263001 (2019).
- [34] H. Cao and J. Wiersig, *Rev. Mod. Phys.* **87**, 61 (2015).
- [35] Z. Zhang, D. Ma, J. Sheng, Y. Zhang, Y. Zhang, and M. Xiao, *J. Phys. B: At., Mol. Opt. Phys.* **51**, 072001 (2018).
- [36] S. K. Gupta, Y. Zou, X.-Y. Zhu, M.-H. Lu, L.-J. Zhang, X.-P. Liu, and Y.-F. Chen, *Adv. Mater.* **32**, 1903639 (2020).
- [37] C. Zeng, Z. Guo, K. Zhu, C. Fan, G. Li, J. Jiang, Y. Li, H. Jiang, Y. Yang, Y. Sun *et al.*, *Chin. Phys. B* **31**, 010307 (2022).
- [38] K. Wang, A. Dutt, K. Y. Yang, C. C. Wojcik, J. Vučković, and S. Fan, *Science* **371**, 1240 (2021).
- [39] G. Ma and P. Sheng, *Sci. Adv.* **2**, e1501595 (2016).
- [40] T. Chou, K. Mallick, and R. K. Zia, *Rep. Prog. Phys.* **74**, 116601 (2011).
- [41] C. M. Bender and S. Boettcher, *Phys. Rev. Lett.* **80**, 5243 (1998).
- [42] E. J. Bergholtz, J. C. Budich, and F. K. Kunst, *Rev. Mod. Phys.* **93**, 015005 (2021).
- [43] M.-A. Miri and A. Alu, *Science* **363**, eaar7709 (2019).
- [44] S. K. Özdemir, S. Rotter, F. Nori, and L. Yang, *Nat. Mater.* **18**, 783 (2019).
- [45] Y. Huang, Y. Shen, C. Min, S. Fan, and G. Veronis, *Nanophotonics* **6**, 977 (2017).
- [46] A. Krasnok, N. Nefedkin, and A. Alù, *IEEE Antennas Propag. Mag.* **63**, 110 (2021).
- [47] A. Banerjee and A. Narayan, *Phys. Rev. B* **102**, 205423 (2020).
- [48] A. Banerjee and A. Narayan, *J. Phys.: Condens. Matter* **33**, 225401 (2021).
- [49] K. Kawabata, T. Bessho, and M. Sato, *Phys. Rev. Lett.* **123**, 066405 (2019).
- [50] W. Hu, H. Wang, P. P. Shum, and Y. D. Chong, *Phys. Rev. B* **95**, 184306 (2017).
- [51] C. Chen, L. Jin, and R.-B. Liu, *New J. Phys.* **21**, 083002 (2019).
- [52] F. Minganti, A. Miranowicz, R. W. Chhajlany, and F. Nori, *Phys. Rev. A* **100**, 062131 (2019).
- [53] V. M. Martinez Alvarez, J. E. Barrios Vargas, and L. E. F. Foa Torres, *Phys. Rev. B* **97**, 121401(R) (2018).
- [54] D. Chowdhury, A. Banerjee, and A. Narayan, *Phys. Rev. A* **103**, L051101 (2021).
- [55] D. Chowdhury, A. Banerjee, and A. Narayan, *Phys. Rev. B* **105**, 075133 (2022).
- [56] M. Parto, Y. G. Liu, B. Bahari, M. Khajavikhan, and D. N. Christodoulides, *Nanophotonics* **10**, 403 (2021).
- [57] B. Midya, H. Zhao, and L. Feng, *Nat. Commun.* **9**, 2674 (2018).
- [58] B. Dietz, H. L. Harney, O. N. Kirillov, M. Miski-Oglu, A. Richter, and F. Schäfer, *Phys. Rev. Lett.* **106**, 150403 (2011).
- [59] C. Dembowski, H.-D. Gräf, H. L. Harney, A. Heine, W. D. Heiss, H. Rehfeld, and A. Richter, *Phys. Rev. Lett.* **86**, 787 (2001).
- [60] Z. Lin, H. Ramezani, T. Eichelkraut, T. Kottos, H. Cao, and D. N. Christodoulides, *Phys. Rev. Lett.* **106**, 213901 (2011).
- [61] H. Hodaei, A. U. Hassan, S. Wittek, H. Garcia-Gracia, R. El-Ganainy, D. N. Christodoulides, and M. Khajavikhan, *Nature (London)* **548**, 187 (2017).
- [62] L. Feng, Z. J. Wong, R.-M. Ma, Y. Wang, and X. Zhang, *Science* **346**, 972 (2014).
- [63] H. Hodaei, M.-A. Miri, M. Heinrich, D. N. Christodoulides, and M. Khajavikhan, *Science* **346**, 975 (2014).
- [64] H. Xu, D. Mason, L. Jiang, and J. Harris, *Nature (London)* **537**, 80 (2016).
- [65] S. Yao and Z. Wang, *Phys. Rev. Lett.* **121**, 086803 (2018).
- [66] F. Song, S. Yao, and Z. Wang, *Phys. Rev. Lett.* **123**, 170401 (2019).
- [67] S. Longhi, *Phys. Rev. Res.* **1**, 023013 (2019).
- [68] L. Li, C. H. Lee, S. Mu, and J. Gong, *Nat. Commun.* **11**, 5491 (2020).
- [69] N. Okuma, K. Kawabata, K. Shiozaki, and M. Sato, *Phys. Rev. Lett.* **124**, 086801 (2020).
- [70] K. Kawabata, M. Sato, and K. Shiozaki, *Phys. Rev. B* **102**, 205118 (2020).
- [71] S. Longhi, *Phys. Rev. B* **102**, 201103(R) (2020).
- [72] L. Li, C. H. Lee, and J. Gong, *Phys. Rev. Lett.* **124**, 250402 (2020).
- [73] M. Lu, X.-X. Zhang, and M. Franz, *Phys. Rev. Lett.* **127**, 256402 (2021).
- [74] D. S. Borgnia, A. J. Kruchkov, and R.-J. Slager, *Phys. Rev. Lett.* **124**, 056802 (2020).
- [75] R. Koch and J. C. Budich, *Eur. Phys. J. D* **74**, 70 (2020).
- [76] F. K. Kunst, E. Edvardsson, J. C. Budich, and E. J. Bergholtz, *Phys. Rev. Lett.* **121**, 026808 (2018).
- [77] L. Xiao, T. Deng, K. Wang, G. Zhu, Z. Wang, W. Yi, and P. Xue, *Nat. Phys.* **16**, 761 (2020).
- [78] E. Edvardsson, F. K. Kunst, and E. J. Bergholtz, *Phys. Rev. B* **99**, 081302(R) (2019).
- [79] Y. Song, W. Liu, L. Zheng, Y. Zhang, B. Wang, and P. Lu, *Phys. Rev. Appl.* **14**, 064076 (2020).
- [80] S. Liu, R. Shao, S. Ma, L. Zhang, O. You, H. Wu, Y. J. Xiang, T. J. Cui, and S. Zhang, *Research* **2021**, 5608038 (2021).
- [81] D. Zou, T. Chen, W. He, J. Bao, C. H. Lee, H. Sun, and X. Zhang, *Nat. Commun.* **12**, 7201 (2021).
- [82] X. Zhang, Y. Tian, J.-H. Jiang, M.-H. Lu, and Y.-F. Chen, *Nat. Commun.* **12**, 5377 (2021).
- [83] L. Zhang, Y. Yang, Y. Ge, Y.-J. Guan, Q. Chen, Q. Yan, F. Chen, R. Xi, Y. Li, D. Jia *et al.*, *Nat. Commun.* **12**, 6297 (2021).
- [84] P. W. Anderson, *Phys. Rev.* **109**, 1492 (1958).
- [85] P. A. Lee and T. Ramakrishnan, *Rev. Mod. Phys.* **57**, 287 (1985).
- [86] B. Kramer and A. MacKinnon, *Rep. Prog. Phys.* **56**, 1469 (1993).
- [87] P. Phillips, *Annu. Rev. Phys. Chem.* **44**, 115 (1993).
- [88] G. Schubert, H. Fehske, L. Fritz, and M. Vojta, *Phys. Rev. B* **85**, 201105(R) (2012).

- [89] M. Segev, Y. Silberberg, and D. N. Christodoulides, *Nat. Photonics* **7**, 197 (2013).
- [90] V. Sacksteder, T. Ohtsuki, and K. Kobayashi, *Phys. Rev. Appl.* **3**, 064006 (2015).
- [91] B. Wu, J. Song, J. Zhou, and H. Jiang, *Chin. Phys. B* **25**, 117311 (2016).
- [92] J. Claes and T. L. Hughes, *Phys. Rev. B* **101**, 224201 (2020).
- [93] R. Sarkar, S. S. Hegde, and A. Narayan, *Phys. Rev. B* **106**, 014207 (2022).
- [94] A. Bandyopadhyay, S. Datta, D. Jana, S. Nath, M. Uddin *et al.*, *Sci. Rep.* **10**, 2502 (2020).
- [95] A. Bandyopadhyay and D. Jana, *Rep. Prog. Phys.* **83**, 056501 (2020).
- [96] W. D. Heiss, *J. Phys. A: Math. Theor.* **45**, 444016 (2012).
- [97] W. Heiss, *J. Phys. A: Math. Gen.* **37**, 2455 (2004).
- [98] S. M. Zhang, X. Z. Zhang, L. Jin, and Z. Song, *Phys. Rev. A* **101**, 033820 (2020).
- [99] R. Jaiswal, A. Banerjee, and A. Narayan, [arXiv:2107.11649](https://arxiv.org/abs/2107.11649).
- [100] Y.-X. Xiao, Z.-Q. Zhang, Z. H. Hang, and C. T. Chan, *Phys. Rev. B* **99**, 241403(R) (2019).
- [101] K. Ding, G. Ma, Z. Q. Zhang, and C. T. Chan, *Phys. Rev. Lett.* **121**, 085702 (2018).
- [102] X. Li, K. Deng, and B. Flebus, *Phys. Rev. B* **106**, 214432 (2022).
- [103] Z. Yang, K. Zhang, C. Fang, and J. Hu, *Phys. Rev. Lett.* **125**, 226402 (2020).
- [104] K. Zhang, Z. Yang, and C. Fang, *Nat. Commun.* **13**, 2496 (2022).
- [105] H. Cai, J. Liu, J. Wu, Y. He, S.-Y. Zhu, J.-X. Zhang, and D.-W. Wang, *Phys. Rev. Lett.* **122**, 023601 (2019).
- [106] T. Stehmann, W. Heiss, and F. Scholtz, *J. Phys. A: Math. Gen.* **37**, 7813 (2004).
- [107] K. Ding, G. Ma, M. Xiao, Z. Q. Zhang, and C. T. Chan, *Phys. Rev. X* **6**, 021007 (2016).
- [108] X.-X. Zhang and M. Franz, *Phys. Rev. Lett.* **124**, 046401 (2020).
- [109] J. Dong, V. Juricic, and B. Roy, *Phys. Rev. Res.* **3**, 023056 (2021).
- [110] Y.-X. Xiao, K. Ding, R.-Y. Zhang, Z. H. Hang, and C. T. Chan, *Phys. Rev. B* **102**, 245144 (2020).
- [111] A. Cerjan, S. Huang, M. Wang, K. P. Chen, Y. Chong, and M. C. Rechtsman, *Nat. Photonics* **13**, 623 (2019).
- [112] M. C. Rechtsman, J. M. Zeuner, Y. Plotnik, Y. Lumer, D. Podolsky, F. Dreisow, S. Nolte, M. Segev, and A. Szameit, *Nature (London)* **496**, 196 (2013).
- [113] Y. Xu, S.-T. Wang, and L.-M. Duan, *Phys. Rev. Lett.* **118**, 045701 (2017).
- [114] S. Longhi, D. Gatti, and G. Della Valle, *Phys. Rev. B* **92**, 094204 (2015).
- [115] C. H. Lee, S. Imhof, C. Berger, F. Bayer, J. Brehm, L. W. Molenkamp, T. Kiessling, and R. Thomale, *Commun. Phys.* **1**, 39 (2018).
- [116] M. Kremer, T. Biesenthal, L. J. Maczewsky, M. Heinrich, R. Thomale, and A. Szameit, *Nat. Commun.* **10**, 435 (2019).
- [117] T. Helbig, T. Hofmann, S. Imhof, M. Abdelghany, T. Kiessling, L. W. Molenkamp, C. H. Lee, A. Szameit, M. Greiter, and R. Thomale, *Nat. Phys.* **16**, 747 (2020).
- [118] Y. Xiong, *J. Phys. Commun.* **2**, 035043 (2018).
- [119] T. E. Lee, *Phys. Rev. Lett.* **116**, 133903 (2016).
- [120] P. Reséndiz-Vázquez, K. Tschernig, A. Perez-Leija, K. Busch, and R. d. J. León-Montiel, *Phys. Rev. Res.* **2**, 013387 (2020).
- [121] X. Z. Zhang and Z. Song, *Phys. Rev. A* **99**, 012113 (2019).
- [122] A. Banerjee, S. S. Hegde, A. Agarwala, and A. Narayan, *Phys. Rev. B* **105**, 205403 (2022).